



# Linear spring stiffnesses for two-dimensional finite element modeling of arteries



J.A. Baier-Saip<sup>a,\*</sup>, P.A. Baier<sup>b</sup>, J.C. Oliveira<sup>c</sup>, H. Baier<sup>d</sup>

<sup>a</sup> Universidad Católica del Maule, Facultad de Ciencias Básicas, Av. San Miguel 3605, Casilla 617, Talca, Chile

<sup>b</sup> Instituto Federal de Educação, Ciência e Tecnologia do Ceará, Rua Estevão Remígio 1145, Limoeiro do Norte, CE, Brazil

<sup>c</sup> Laboratório Nacional de Computação Científica, Av. Getúlio Vargas 333, Petrópolis, RJ, Brazil

<sup>d</sup> Universität Würzburg, am Hubland, 97074 Würzburg, Germany

## ARTICLE INFO

### Keywords:

Elasticity tensor  
Normal and angular springs  
Stiffnesses

## ABSTRACT

The physical properties of arteries are important in the research of the circulatory system dynamics. Moreover, in order to build Virtual Reality Simulators, it is crucial to have a tissue model able to respond in real time. A reduced mesh size results in shorter processing times, which can be achieved using a two-dimensional grid. In this work, a triangular topology is considered and the nodes are connected by three kinds of linear springs (one normal and two angular ones). The spring stiffnesses depend on the mesh geometry and on the elastic properties of the artery. The model linearizes the material response, but it still contemplates the geometric nonlinearities. Comparisons showed a good match with a nonlinear model and with our previous model based on a quadrilateral topology. However, the proposed model extension is more flexible and easier to implement than the previous one.

## 1. Introduction

Conducting clinical research is expensive, time-consuming, and manipulating biological variables is very challenging (Gwak et al., 2010). Although mathematical modeling may be difficult in some cases, virtual cardiovascular simulations are inexpensive and variables can be easily controlled (Zannoli et al., 2009). For example, studies of atherosclerotic plaques have evaluated the 3D stress distributions within plaques under certain loading and boundary conditions, so to analyze the biomechanical response to geometrical, structural, and material changes (Creane et al., 2010; Cilla et al., 2012; Morlacchi et al., 2013; Holzapfel et al., 2014).

A better understanding of the arterial wall mechanics can provide relevant information for medical diagnosis and therapies of some vascular pathologies (Garcia-Herrera et al., 2012). Indeed, the measurements of the arterial tree stiffness can be applied in routine clinical practice for risk stratification (Pereira et al., 2015). Detailed knowledge of vascular tissue properties is required to improve procedures such as angioplasty, to design arterial prostheses, and to describe the dynamics of the interaction between the heart and the circulatory system (Holzapfel et al., 2002). Moreover, physiological and pathological changes in the cardiovascular system directly influence the mechanical behavior of arterial walls (Diez, 2007).

The arterial wall is incompressible, anisotropic, inhomogeneous, highly nonlinear, and exhibits hysteresis under a cyclic load (Holzapfel and Ogden, 2010; Li, 2016). Usually, only the passive behavior of the tissue is considered, but even so, a complex set of equations results and a considerable amount of processing time is used to obtain the solution.

In order to show the artery deformations caused by the introduction of medical devices, a truthful Virtual Reality Simulator (VRS) must consider the physical models of the device and of the artery (Alderliesten et al., 2007; Wang et al., 2014; Baier et al., 2015, 2016). Due to its strong mathematical background, Finite Element Methods (FEM) are physically accurate (Garcia et al., 2006) and linear FEM are the most popular technique to model tissue deformation in VRS (Misra et al., 2008). The FEM have shown to be robust for the quantification of arterial stresses, and they have been successfully utilized for modeling of the stent-artery interaction. Balloon expandable stents have also been compared with self-expanding stents in terms of the level of stresses they induce within the arterial wall, and hence the risk of arterial injury.

A VRS must work in real time. For example, a haptic device demands a minimum refresh rate of 500 Hz, so that the user can experience a continuous (smooth) contact feeling. Thus, the reaction force due to tissue deformations has to be calculated very quickly. Although commercially available finite element codes take into account several

\* Corresponding author.

E-mail address: [jbaier@ucm.cl](mailto:jbaier@ucm.cl) (J.A. Baier-Saip).

physical aspects of arteries (including nonlinearities), the computation time would be too long for VRS. The model developed in this paper is intended to be used in fast calculations of artery deformations, where an exact response is not necessary.

In particular, the artery deformations produced by a catheter wire are tiny, and in this case the linear approximation is adequate. Hence, linearizations are adopted in the calculations of the elasticity tensor and of the spring stiffnesses. Furthermore, the method is based on a structural mechanic approach, because a VRS only requires the force feedback at the contact points and not the knowledge e.g. of a stress field at the surface.

A two-dimensional mesh is proposed and so the numerical difficulties arising from the isochoric constrain in three dimensions are avoided. This paper is organized as follows, in Section 2 the stiffness tensor component  $C_{\eta\eta\eta\eta}$  is estimated, from which  $C_{\theta z\theta z}$  can be calculated. Furthermore, the interaction between the nodes is simulated using normal, angular in plane, and angular out of plane springs. Then, in Section 3 the stiffnesses are determined and the results are analyzed.

## 2. Methods

When accuracy is not the most relevant aspect, a reduced mesh size and a linearization increase the computing performance. The model developed in this work is equivalent to a linear FEM using a triangular mesh with few nodes. First, additional stiffness tensor components are estimated and, afterwards, the formulas for calculating the stiffness of the springs are deduced.

### 2.1. Stiffness tensor

Fiber dispersion in collagenous soft tissues has an important influence on the mechanical response (Holzapfel and Ogden, 2017). There exist two different approaches for modeling fiber dispersion: the “angular integration” (Lanir, 1983) and the “generalized structure tensor” (Gasser et al., 2006). Both models have equivalent predictive power, and from the theoretical point of view neither of these models is superior to the other. However, the generalized structure tensor has proved to be very successful in modeling the data from experiments on a wide range of tissues. Furthermore, it is easier to analyze, simpler to implement, and the related computational effort is much lower than the angular integration approach.

Holzapfel et al. (2015) provide an overview of the main existing continuum nonlinear mechanical models of arteries, which have proven to give reliable results. In general, classical continuum mechanics assumes that the constitutive models and the corresponding simulations start from an unloaded, stress-free reference configuration (Pierce et al., 2015). This has been used to calculate the amount of stress applied to the tissue and its associated strain response (Fung, 1993; Humphrey, 2002; Vito and Dixon, 2003; Sokolis, 2008).

However, the boundary value problem of interest represents a loaded geometry and includes residual stresses. It has been shown that residual stresses make the stress distribution more homogeneous within each arterial layer (Fung, 1991). The modeling of residual deformations take into account the stress and bending, which are axially dependent. In order to take into account the residual stretches in our model, it would be necessary to calculate in a previous step the stresses and prestresses using a continuum mechanics approach (Pierce et al., 2015). Then the resulting stretches can be used to compute the inhomogeneous stiffness tensor (see below), which in turn is used to compute volume averages (Section 2.2). Nevertheless, this will not be pursued mainly because in our model only a two-dimensional picture is obtained, and the stress variation within a layer cannot be observed.

Usually, only planar biaxial deformations (tangential stretch  $\lambda_\theta$  and axial stretch  $\lambda_z$ ) are performed in experiments to obtain the most relevant information about the material properties. Nonetheless, this is not sufficient to characterize all material properties of soft tissues

(Holzapfel and Ogden, 2009). In the present work, the energy density function for the arterial layer  $\mathbf{t}$  (Intima, Media, or Adventitia) is given by

$$\Psi_{\mathbf{t}} = \mu_{\mathbf{t}}(I_{\mathbf{t}} - 3) + \frac{k_{1\mathbf{t}}}{k_{2\mathbf{t}}}(\Gamma_{\mathbf{t}} - 1), \quad (1)$$

where

$$\Gamma_{\mathbf{t}} = e^{k_{2\mathbf{t}}[(1-\rho_{\mathbf{t}})(I_{\mathbf{t}}-3)^2 + \rho_{\mathbf{t}}(I_{4\mathbf{t}}-1)^2]}. \quad (2)$$

Further, the invariants  $I_{\mathbf{t}}$ ,  $I_{4\mathbf{t}}$  are defined by

$$I_{\mathbf{t}} = \lambda_\theta^2 + \lambda_z^2 + \frac{1}{\lambda_\theta^2 \lambda_z^2},$$

$$I_{4\mathbf{t}} = \lambda_\theta^2 \cos^2 \phi_{\mathbf{t}} + \lambda_z^2 \sin^2 \phi_{\mathbf{t}}, \quad (3)$$

and the physical parameters of the layers  $\mu_{\mathbf{t}}$ ,  $k_{1\mathbf{t}}$ ,  $k_{2\mathbf{t}}$ ,  $\rho_{\mathbf{t}}$ ,  $\phi_{\mathbf{t}}$  were experimentally obtained from the coronaries of human cadavers (Holzapfel et al., 2005). In particular, the energy density invariants capture structural aspects of the tissue (e.g. the orientation and dispersion of collagen fibers).

The stiffness tensor components  $C_{\theta\theta\theta\theta}$ ,  $C_{zzzz}$ , and  $C_{\theta z\theta z}$  of layer  $\mathbf{t}$  were determined in Ref. (Baier-Saip et al., 2017). However, the calculations of the angular spring stiffnesses (Section 2.2) require also the knowledge of the tensor component  $C_{\eta\eta\eta\eta}$ . In order to find  $C_{\eta\eta\eta\eta}$ , it is necessary to write the stretches  $\lambda_\theta$  and  $\lambda_z$  appearing in the energy density in terms of  $\lambda_{\parallel}$  (the stretch parallel to the vector  $\mathbf{e}_{\parallel}$ , see Fig. 1). To this end, consider the point  $A_0$  with coordinate (1,1). If the body is subjected to an initial deformation specified by the stretches  $\lambda_{\theta 0}$  and  $\lambda_{z 0}$ , the new coordinate will be  $(\lambda_{\theta 0}, \lambda_{z 0})$  (point  $A_1$ ). After displacing this point a distance  $\delta$  in the direction of  $\mathbf{e}_{\parallel}$  the coordinate becomes  $(\lambda_{\theta 0} + \delta \cos \eta, \lambda_{z 0} + \delta \sin \eta)$  (point  $A_2$ ). The stretch ratio equals the final length divided by the initial length parallel to the axis, which is equal to 1

$$\lambda_\theta = \lambda_{\theta 0} + \delta \cos \eta,$$

$$\lambda_z = \lambda_{z 0} + \delta \sin \eta.$$

Moreover, the projections of the segments  $\overline{OA_0}$  and  $\overline{OA_2}$  along the vector  $\mathbf{e}_{\parallel}$ , are  $\cos \eta + \sin \eta$  and  $\lambda_{\theta 0} \cos \eta + \lambda_{z 0} \sin \eta + \delta$  respectively. Thus, the stretch ratio is

$$\lambda_{\parallel} = \frac{\lambda_{\theta 0} \cos \eta + \lambda_{z 0} \sin \eta + \delta}{\cos \eta + \sin \eta} = \frac{\lambda_\theta \cos \eta + \lambda_z \sin \eta}{\cos \eta + \sin \eta}. \quad (4a)$$

The projections of the segments  $\overline{OA_0}$  and  $\overline{OA_2}$  along the vector  $\mathbf{e}_{\perp} = -\sin \eta \mathbf{e}_\theta + \cos \eta \mathbf{e}_z$  perpendicular to  $\mathbf{e}_{\parallel}$ , are  $\cos \eta - \sin \eta$  and

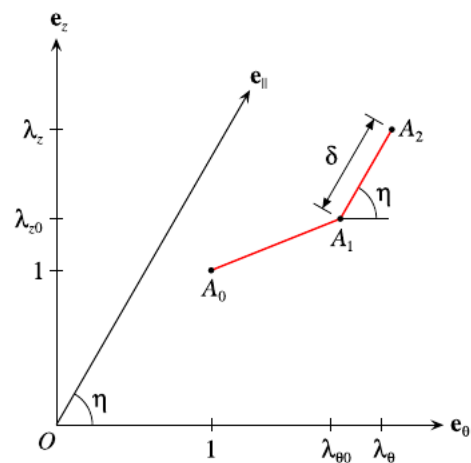


Fig. 1. Coordinates of a point in a body without stretch (point  $A_0$ ), with an initial stretch (point  $A_1$ ), and after an additional deformation parallel to  $\mathbf{e}_{\parallel}$  (point  $A_2$ ). The unit vector  $\mathbf{e}_{\parallel}$  is in the plane of  $\mathbf{e}_\theta$  and  $\mathbf{e}_z$ . Besides, the angle between  $\mathbf{e}_{\parallel}$  and  $\mathbf{e}_\theta$  is  $\eta$ .

$\lambda_{z0}\cos\eta - \lambda_{\theta0}\sin\eta$  respectively. The stretch ratio

$$\lambda_{\perp} = \frac{\lambda_{z0}\cos\eta - \lambda_{\theta0}\sin\eta}{\cos\eta - \sin\eta} = \frac{\lambda_z\cos\eta - \lambda_{\theta}\sin\eta}{\cos\eta - \sin\eta}. \quad (4b)$$

does not depend on  $\delta$ . Henceforth,  $\lambda_{\perp}$  is implicitly constant.

Solving for  $\lambda_{\theta}$  and  $\lambda_z$  from (4a) and (4b), it is found that

$$\lambda_{\theta} = \lambda'_{\parallel}\cos\eta - \lambda'_{\perp}\sin\eta, \quad (5)$$

$$\lambda_z = \lambda'_{\parallel}\sin\eta + \lambda'_{\perp}\cos\eta,$$

where  $\lambda'_{\parallel} = \lambda_{\parallel}(\cos\eta + \sin\eta)$  and  $\lambda'_{\perp} = \lambda_{\perp}(\cos\eta - \sin\eta)$ . Furthermore, let

$$\lambda'_r = \frac{1}{\lambda_{\theta}\lambda_z} = \frac{1}{\frac{1}{2}(\lambda'^2_{\parallel} - \lambda'^2_{\perp})\sin 2\eta + \lambda'_{\parallel}\lambda'_{\perp}\cos 2\eta} \quad (6)$$

In this way, the invariants in (3) become

$$I_1 = \lambda'^2_{\parallel} + \lambda'^2_{\perp} + \lambda'^2_r, \quad (7)$$

$$I_{4t} = (\lambda'_{\parallel}\cos\eta - \lambda'_{\perp}\sin\eta)^2\cos^2\phi_t + (\lambda'_{\parallel}\sin\eta + \lambda'_{\perp}\cos\eta)^2\sin^2\phi_t$$

The stress is calculated as

$$\sigma_{\eta\eta t} = \lambda_{\parallel} \frac{\partial \Psi_t}{\partial \lambda_{\parallel}} = \lambda'_{\parallel} \frac{\partial \Psi_t}{\partial \lambda'_{\parallel}}$$

and the stiffness tensor component is

$$C_{\eta\eta\eta t} = \lambda'_{\parallel} \frac{\partial \sigma_{\eta\eta t}}{\partial \lambda'_{\parallel}} = \lambda'_{\parallel} \frac{\partial \sigma_{\eta\eta t}}{\partial \lambda'_{\parallel}}$$

Introducing the definitions

$$P = \lambda'_{\parallel} \frac{\partial I_1}{\partial \lambda'_{\parallel}} = 2\lambda'^2_{\parallel} - 2\lambda'^3_r(\lambda'^2_{\parallel}\sin 2\eta + \lambda'_{\parallel}\lambda'_{\perp}\cos 2\eta),$$

$$Q_t = \lambda'_{\parallel} \frac{\partial I_{4t}}{\partial \lambda'_{\parallel}} = 2\lambda'_{\parallel}(\lambda_{\theta}\cos\eta \cos^2\phi_t + \lambda_z\sin\eta \sin^2\phi_t),$$

$$X = \lambda'_{\parallel} \frac{\partial P}{\partial \lambda'_{\parallel}} = 4\lambda'^2_{\parallel} - 2\lambda'^3_r(2\lambda'^2_{\parallel}\sin 2\eta + \lambda'_{\parallel}\lambda'_{\perp}\cos 2\eta) + 6\lambda'^4_r(\lambda'^2_{\parallel}\sin 2\eta + \lambda'_{\parallel}\lambda'_{\perp}\cos 2\eta)^2,$$

$$Y_t = \lambda'_{\parallel} \frac{\partial Q_t}{\partial \lambda'_{\parallel}} = 2\lambda'_{\parallel}(\lambda_{\theta}\cos\eta \cos^2\phi_t + \lambda_z\sin\eta \sin^2\phi_t) + 2\lambda'^2_{\parallel}(\cos^2\eta \cos^2\phi_t + \sin^2\eta \sin^2\phi_t), \quad (8)$$

it follows that

$$C_{\eta\eta\eta t} = \mu_t X + 4k_t k_t \Gamma_t [(1 - \rho_t)(I_1 - 3)P + \rho_t(I_{4t} - 1)Q_t] + 2k_t \Gamma_t [(1 - \rho_t)P^2 + \rho_t Q_t^2 + (1 - \rho_t)(I_1 - 3)X + \rho_t(I_{4t} - 1)Y_t]. \quad (9)$$

In particular, for  $\eta = 0^\circ$  and  $\eta = 90^\circ$  the last equation simplifies to  $C_{\eta\eta\eta t} = C_{\theta\theta\theta t}$  and  $C_{\eta\eta\eta t} = C_{zzz t}$  respectively, see Ref. (Baier-Saip et al., 2017).

Next, consider the calculation of  $C_{\theta z \theta z t}$ . Suppose that  $C_{\theta\theta\theta t}$ ,  $C_{zzz t}$ ,  $C_{\theta\theta z z t}$  have been obtained as described in Ref. (Baier-Saip et al., 2017), and  $C_{\frac{\pi}{4} \frac{\pi}{4} \frac{\pi}{4} \frac{\pi}{4} t}$  has been obtained using (9) with  $\eta = 45^\circ$ . Since in a rotation the tensor component can also be calculated with the formula  $C_{\frac{\pi}{4} \frac{\pi}{4} \frac{\pi}{4} \frac{\pi}{4} t} = \frac{1}{4} C_{\theta\theta\theta t} + \frac{1}{4} C_{zzz t} + \frac{1}{2} C_{\theta\theta z z t} + C_{\theta z \theta z t}$ , it follows that

$$C_{\theta z \theta z t} = C_{\frac{\pi}{4} \frac{\pi}{4} \frac{\pi}{4} \frac{\pi}{4} t} - \frac{1}{4} C_{\theta\theta\theta t} - \frac{1}{4} C_{zzz t} - \frac{1}{2} C_{\theta\theta z z t} \quad (10)$$

## 2.2. Spring stiffnesses

In order to simulate the physical properties of the tissues, the nodes located at the inner surface of the Intima are connected with three kinds of linear springs:

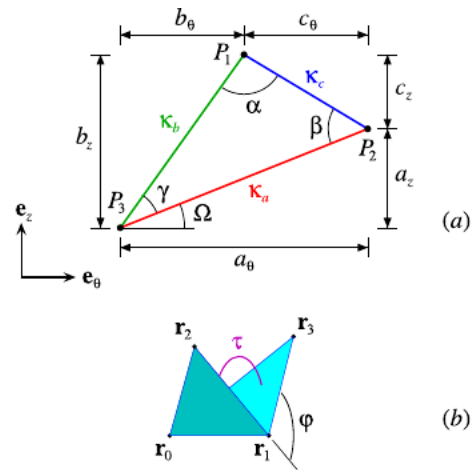


**Fig. 2.** (a) Three nodes (black points  $P_1, P_2, P_3$ ) are connected by springs of stiffness  $\kappa_c$  (red line),  $\kappa_b$  (green line), and  $\kappa_a$  (blue line). There are also angular springs  $\chi_\alpha, \chi_\beta$  and  $\chi_\gamma$  (not shown) at the vertices  $P_1, P_2$ , and  $P_3$  respectively. The vertex  $P_3$  is at the origin, so that the coordinates of  $P_2$  and  $P_1$  are  $(a_\theta, a_z)$  and  $(b_\theta, b_z)$  respectively. The angle between the segment  $P_2P_3$  and the tangential direction  $\mathbf{e}_\theta$  is  $\Omega$ . Deforming the triangle changes the lengths  $a = \sqrt{a_\theta^2 + a_z^2}$ ,  $b = \sqrt{b_\theta^2 + b_z^2}$ ,  $c = \sqrt{c_\theta^2 + c_z^2}$ , and the angles  $\alpha, \beta, \gamma$ . (b) Two adjacent triangles with vertices at  $\mathbf{r}_0, \mathbf{r}_1, \mathbf{r}_2$  and at  $\mathbf{r}_0, \mathbf{r}_1, \mathbf{r}_3$ , have attached one angular spring of stiffness  $\tau$  (magenta arc) between the planes, i.e. between the surface normals. (For interpretation of the references to colour in this figure legend, the reader is referred to the Web version of this article.)

1. *Normal spring* with stiffness  $\kappa_i$  and energy  $\kappa_i(\Delta x_i)^2/2$ , where  $\Delta x_i$  represents the deviation from the equilibrium distance  $x_i = a, b, c$  between two nodes (Fig. 2(a)).
2. *Angular in plane spring* with stiffness  $\chi_i$  and energy  $\chi_i(\Delta \omega_i)^2/2$ , where  $\omega_i = \alpha, \beta, \gamma$  are the angles in the triangle (Fig. 2(a)).
3. *Angular out of plane spring* with stiffness  $\tau$  and energy  $\tau(\Delta[\sin\phi])^2/2$ , which is associated with the angle  $\phi$  between two neighboring triangles (Fig. 2(b)). This angle depends on the relative position of four nodes.

Although the model linearizes the material response in the springs, it still contemplates the geometric nonlinearity by updating the reference frame to the deformed geometry in the calculations (Baier-Saip et al., 2017).

### 2.2.1. Normal springs $\kappa_i$ and angular in plane springs $\chi_i$

The stiffness of the springs  $\kappa_i$  and  $\chi_i$  is related to the elastic properties of the tissues and to the geometry of the mesh. If the triangle in Fig. 2(a) is subjected to the strains  $\epsilon_{\theta\theta}$ ,  $\epsilon_{zz}$ , and  $\epsilon_{\theta z}$ , then the deviation of the lengths from equilibrium are to first order

$$\Delta a = \frac{a_\theta^2 \epsilon_{\theta\theta} + a_z^2 \epsilon_{zz} + 2a_\theta a_z \epsilon_{\theta z}}{a},$$

$$\Delta b = \frac{b_\theta^2 \epsilon_{\theta\theta} + b_z^2 \epsilon_{zz} + 2b_\theta b_z \epsilon_{\theta z}}{b},$$

$$\Delta c = \frac{c_\theta^2 \epsilon_{\theta\theta} + c_z^2 \epsilon_{zz} + 2c_\theta c_z \epsilon_{\theta z}}{c}. \quad (11)$$

Moreover, the deviation of the angles are

$$\Delta \alpha = M_{bc}(\epsilon_{\theta\theta} - \epsilon_{zz}) + N_{bc}\epsilon_{\theta z},$$

$$\Delta \beta = M_{ca}(\epsilon_{\theta\theta} - \epsilon_{zz}) + N_{ca}\epsilon_{\theta z},$$

$$\Delta \gamma = M_{ab}(\epsilon_{\theta\theta} - \epsilon_{zz}) + N_{ab}\epsilon_{\theta z}, \quad (12)$$

where

$$\begin{aligned}
 M_{bc} &= \frac{b_\theta b_z}{b^2} - \frac{c_\theta c_z}{c^2}, N_{bc} = \frac{b_\theta^2 - b_z^2}{b^2} - \frac{c_\theta^2 - c_z^2}{c^2}, \\
 M_{ca} &= \frac{c_\theta c_z}{c^2} - \frac{a_\theta a_z}{a^2}, N_{ca} = \frac{c_\theta^2 - c_z^2}{c^2} - \frac{a_\theta^2 - a_z^2}{a^2}, \\
 M_{ab} &= \frac{a_\theta a_z}{a^2} - \frac{b_\theta b_z}{b^2}, N_{ab} = \frac{a_\theta^2 - a_z^2}{a^2} - \frac{b_\theta^2 - b_z^2}{b^2}.
 \end{aligned} \tag{12a}$$

note that  $M_{ij}$ ,  $N_{ij}$  depend on the shape and orientation of the triangle, but they do not depend on its size.

The energy stored in the springs is

$$\begin{aligned}
 U_\varepsilon &= \frac{1}{2} \kappa_a (\Delta a)^2 + \frac{1}{2} \kappa_b (\Delta b)^2 + \frac{1}{2} \kappa_c (\Delta c)^2 + \frac{1}{2} \chi_\alpha (\Delta \alpha)^2 + \frac{1}{2} \chi_\beta (\Delta \beta)^2 \\
 &+ \frac{1}{2} \chi_\gamma (\Delta \gamma)^2.
 \end{aligned} \tag{13}$$

On the other hand, the elastic energy due to the deformation of the tissue is

$$U_\varepsilon = \frac{1}{2} F_{\theta\theta\theta\theta} \varepsilon_{\theta\theta}^2 + \frac{1}{2} F_{zzzz} \varepsilon_{zz}^2 + F_{\theta z z z} \varepsilon_{\theta\theta} \varepsilon_{zz} + 2 F_{\theta z \theta z} \varepsilon_{\theta z}^2, \tag{14}$$

where

$$\bar{F}_{ijkl} = \int_V C_{ijkl} dV \tag{14a}$$

is the integral of the stiffness over the volume  $V$  bounded by a triangular prism, which includes the Intima, Media, and Adventitia tissues.

By comparing the coefficients of  $\varepsilon_{\theta\theta}^2$ ,  $\varepsilon_{zz}^2$ ,  $\varepsilon_{\theta z}^2$ ,  $\varepsilon_{\theta\theta} \varepsilon_{zz}$ ,  $\varepsilon_{\theta z} \varepsilon_{\theta z}$ ,  $\varepsilon_{zz} \varepsilon_{\theta z}$  in (13) and (14), the following equations are obtained after a slight manipulation

$$\begin{aligned}
 a_\theta^2 \kappa_a + b_\theta^2 \kappa_b + c_\theta^2 \kappa_c &= F_{\theta\theta\theta\theta} + F_{\theta z z z}, \\
 a_z^2 \kappa_a + b_z^2 \kappa_b + c_z^2 \kappa_c &= F_{zzzz} + F_{\theta z z z}, \\
 a_\theta a_z \kappa_a + b_\theta b_z \kappa_b + c_\theta c_z \kappa_c &= 0,
 \end{aligned} \tag{15a}$$

and

$$\begin{aligned}
 M_{bc}^2 \chi_\alpha + M_{ca}^2 \chi_\beta + M_{ab}^2 \chi_\gamma &= \frac{a_\theta^2 a_z^2}{a^2} \kappa_a + \frac{b_\theta^2 b_z^2}{b^2} \kappa_b + \frac{c_\theta^2 c_z^2}{c^2} \kappa_c - F_{\theta z \theta z}, \\
 N_{bc}^2 \chi_\alpha + N_{ca}^2 \chi_\beta + N_{ab}^2 \chi_\gamma &= -4 \left( \frac{a_\theta a_z^2}{a^2} \kappa_a + \frac{b_\theta b_z^2}{b^2} \kappa_b + \frac{c_\theta^2 c_z^2}{c^2} \kappa_c - F_{\theta z \theta z} \right), \\
 M_{bc} N_{bc} \chi_\alpha + M_{ca} N_{ca} \chi_\beta + M_{ab} N_{ab} \chi_\gamma &= 2 a_\theta a_z \frac{a_z^2 - a_\theta^2}{a^2} \kappa_a + 2 b_\theta b_z \frac{b_z^2 - b_\theta^2}{b^2} \kappa_b \\
 &+ 2 c_\theta c_z \frac{c_z^2 - c_\theta^2}{c^2} \kappa_c.
 \end{aligned} \tag{15b}$$

Equation (15a) is solved first to obtain  $\kappa_a$ ,  $\kappa_b$ ,  $\kappa_c$ , and then these values are substituted in (15b) to obtain  $\chi_\alpha$ ,  $\chi_\beta$ ,  $\chi_\gamma$ . Note that the structure of both equations is similar.

### 2.2.2. Angular out of plane spring $\tau$

Consider a homogeneous beam with a natural curvature radius  $R_0$  and a thickness  $h$ . When the beam is subjected to a deformation specified by a new radius  $R$ , the bending energy equals

$$U_{\text{bend},\eta} = \frac{1}{2} \left( \frac{1}{R} - \frac{1}{R_0} \right)^2 g_\eta V_{2+3}, \tag{16}$$

where  $g_\eta = C_{\eta\eta\eta\eta} h^2/12$  and  $V_{2+3}$  is the volume bounded by the two triangular prisms.

It can be inferred from Fig. 3 that  $d = 2R \sin(\varphi/2)$ , where  $d = d_2$  represents the distance from  $\mathbf{r}_2$  to the line through the points  $\mathbf{r}_0$  and  $\mathbf{n}_1$  (parallel to  $\mathbf{n}_1$ ). Equivalently,  $d = d_3$  represents the distance from  $\mathbf{r}_3$  to the same line. Later, the case  $d_2 \neq d_3$  will be taken into account. Observe that

$$\frac{1}{R} - \frac{1}{R_0} = \frac{2}{d} \left( \sin \frac{\varphi}{2} - \sin \frac{\varphi_0}{2} \right), \tag{17}$$

where  $\varphi_0$  is the angle between the planes in the undeformed state. If  $\varphi$  is close to  $\varphi_0$ , then up to first order in  $\Delta\varphi = \varphi - \varphi_0$

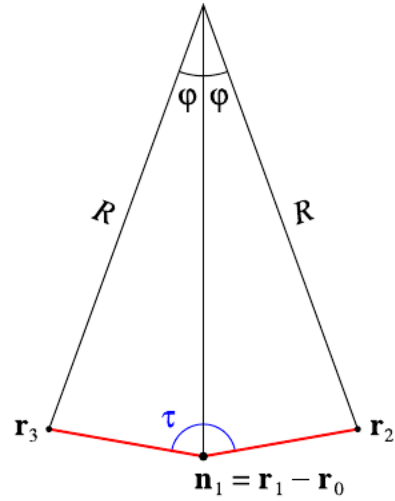


Fig. 3. Cross view of two adjacent triangles (red) perpendicular to the plane of the Figure, with a common axis of rotation parallel to the vector  $\mathbf{n}_1$  (represented by the dot  $\bullet$ ). When the triangles are rotated, the structure is bent with a curvature radius  $R$ . The stiffness of the angular spring connected to the triangles is  $\tau$  (blue). (For interpretation of the references to colour in this figure legend, the reader is referred to the Web version of this article.)

$$2 \left( \sin \frac{\varphi}{2} - \sin \frac{\varphi_0}{2} \right) = \Delta\varphi \cos \frac{\varphi_0}{2} = \frac{\cos^2 \frac{\varphi_0}{2}}{\cos^2 \varphi_0} (\sin\varphi - \sin\varphi_0). \tag{18}$$

substituting (17) and (18) in (16)

$$U_{\text{bend},\eta} = \frac{1}{2} g_\eta \frac{V_{2+3}}{d^2} \frac{\cos^2 \frac{\varphi_0}{2}}{\cos^2 \varphi_0} (\sin\varphi - \sin\varphi_0)^2. \tag{19}$$

On the other hand, the energy stored in the angular spring connected to the triangles is

$$U_{\text{bend},\eta} = \frac{1}{2} \tau (\Delta[\sin\varphi])^2. \tag{20}$$

hence, from (19) and (20)

$$\tau = g_\eta \frac{V_{2+3}}{d^2} \frac{\cos^2 \frac{\varphi_0}{2}}{\cos^2 \varphi_0}. \tag{21a}$$

If the two triangles are not isometric (i.e.  $d_2 \neq d_3$ ), using the same angle  $\varphi$  but with different radii  $R_2$  and  $R_3$ , the relations  $d_2 = 2R_2 \sin(\varphi/2)$  and  $d_3 = 2R_3 \sin(\varphi/2)$  are obtained. Hence, (21a) is replaced by

$$\tau = g_\eta \left( \frac{V_2}{d_2^2} + \frac{V_3}{d_3^2} \right) \frac{\cos^2 \frac{\varphi_0}{2}}{\cos^2 \varphi_0}. \tag{21b}$$

Finally, when the beam is not homogeneous (e.g. due to variations of the stiffness tensor), the last equation becomes

$$\tau = \left( \frac{G_{\eta 2}}{d_2^2} + \frac{G_{\eta 3}}{d_3^2} \right) \frac{\cos^2 \frac{\varphi_0}{2}}{\cos^2 \varphi_0}. \tag{21c}$$

here

$$G_{\eta i} = \int_{V_i} y^2 C_{\eta\eta\eta\eta} dV, \tag{21d}$$

where  $y$  denotes the distance to the neutral axis of the beam.

Next, define the vectors

$$\begin{aligned}
 \mathbf{n}_1 &= \mathbf{r}_1 - \mathbf{r}_0, \\
 \mathbf{n}_2 &= \mathbf{n}_1 \times (\mathbf{r}_2 - \mathbf{r}_0), \\
 \mathbf{n}_3 &= (\mathbf{r}_3 - \mathbf{r}_0) \times \mathbf{n}_1, \\
 \mathbf{n}_4 &= (\mathbf{r}_3 - \mathbf{r}_0) \times (\mathbf{r}_2 - \mathbf{r}_0),
 \end{aligned} \tag{22}$$

and let  $n_i = |\mathbf{n}_i|$  represent their modulus. Then

$$\sin \varphi = \frac{\mathbf{n}_1 \cdot (\mathbf{n}_2 \times \mathbf{n}_3)}{n_1 n_2 n_3}. \quad (23)$$

Furthermore, a helpful formula for the derivation of the stiffness matrix used in FEM is

$$\delta(\sin \varphi) = \nabla_0(\sin \varphi) \cdot \delta \mathbf{r}_0 + \nabla_1(\sin \varphi) \cdot \delta \mathbf{r}_1 + \nabla_2(\sin \varphi) \cdot \delta \mathbf{r}_2 + \nabla_3(\sin \varphi) \cdot \delta \mathbf{r}_3, \quad (24)$$

with

$$\begin{aligned} \nabla_0(\sin \varphi) &= \frac{n_1^2(\mathbf{n}_2 + \mathbf{n}_3 - \mathbf{n}_4) - 2\mathbf{n}_1(\mathbf{n}_2 \cdot \mathbf{n}_3)}{n_1 n_2 n_3} + \sin \varphi \left[ \frac{\mathbf{n}_1}{n_1^2} - \frac{\mathbf{n}_2 \times (\mathbf{r}_2 - \mathbf{r}_1)}{n_2^2} \right. \\ &\quad \left. - \frac{(\mathbf{r}_3 - \mathbf{r}_1) \times \mathbf{n}_3}{n_3^2} \right], \\ \nabla_1(\sin \varphi) &= \frac{2\mathbf{n}_1(\mathbf{n}_2 \cdot \mathbf{n}_4) + n_1^2 \mathbf{n}_4}{n_1 n_2 n_3} + \sin \varphi \left[ -\frac{\mathbf{n}_1}{n_1^2} + \frac{\mathbf{n}_2 \times (\mathbf{r}_2 - \mathbf{r}_0)}{n_2^2} + \frac{(\mathbf{r}_3 - \mathbf{r}_0) \times \mathbf{n}_3}{n_3^2} \right], \\ \nabla_2(\sin \varphi) &= -\frac{n_1}{n_2 n_3} \mathbf{n}_3 + \sin \varphi \frac{\mathbf{n}_1 \times \mathbf{n}_2}{n_2^2}, \\ \nabla_3(\sin \varphi) &= -\frac{n_1}{n_2 n_3} \mathbf{n}_2 + \sin \varphi \frac{\mathbf{n}_3 \times \mathbf{n}_1}{n_3^2}. \end{aligned} \quad (24a)$$

If the angular out of plane spring is omitted from the model, then the stiffness matrix can be singular. Physically, the structure is not stable when there is no restoring force in a direction perpendicular to the plane of the triangles.

### 3. Results

As an application of the theory developed in Section 2, first the stiffness tensor for a symbolic artery is obtained, and then the effect of the mesh geometry on the spring stiffnesses is studied. In particular, the angular energies proportional to  $[\Delta \sin \varphi]^2$  and to  $[\Delta \cos \varphi]^2$  are compared.

The model is contrasted in three different cases which have been investigated in Ref. (Baier-Saip et al., 2017). Finally, the model is applied to an artery with inhomogeneous properties representing a damaged artery.

#### 3.1. Physical parameters

In general, the artery stiffness among different individuals has large variations (Schmid et al., 2013) and the data in Table 1 is used to calculate typical values of the stiffness tensor components.

Assuming a mean pressure loading equal to  $(80 + 120)/2 = 100$  mm Hg and no residual strains, the calculated stretch at the inner surface is  $\lambda_{\theta \text{in}} = 1.1495$  and the internal radius is  $r_1 = 1.55$  mm (Baier-Saip et al., 2017). The resulting volume averages of the stiffness tensor components are given in Table 2. This table also contains the results when the artery (a cylinder) is replaced by a planar slice of total thickness  $0.24 + 0.32 + 0.34 = 0.90$  mm and there is no internal pressure, so that  $\lambda_\theta = 1$ .

Physically, the collagen fibers are on average closer to  $45^\circ$  than  $0^\circ$  or  $90^\circ$  (see  $\phi_t$  in Table 1). Hence,  $C_{\frac{\pi}{4}\frac{\pi}{4}\frac{\pi}{4}\frac{\pi}{4}}$  is much bigger than  $C_{\theta\theta\theta\theta}$  and  $C_{zzzz}$ . So, according to (10) the value of  $C_{\theta z \theta z t}$  must be considerably larger than the other tensor components, as confirmed in Table 2. Lastly, in Table 3 are the values of  $\bar{g}_\eta$  for different angles  $\eta$ , which will

**Table 1**

Average physical parameters from Ref. (Holzapfel et al., 2005) for the Intima (i), Media (m), and Adventitia (a) arterial layers. The thickness  $a_t$  is in mm,  $\mu_t$  and  $k_{1t}$  are in kPa,  $k_{2t}$  are dimensionless, and the angle  $\phi_t$  is in degrees. Furthermore, the internal radius without pressure loading is 1.35 mm.

t	$a_t$	$\mu_t$	$k_{1t}$	$k_{2t}$	$\rho_t$	$\phi_t$
i	0.24	27.90	263.66	170.88	0.51	$60.3^\circ$
m	0.32	1.27	21.60	8.21	0.25	$20.6^\circ$
a	0.34	7.56	38.57	85.03	0.55	$67.0^\circ$

**Table 2**

Average components of the stiffness tensor  $\bar{C}_{ijkl}$  (in kPa) for two different geometries and internal pressures  $p_{\text{in}}$  (in mmHg).

Geometry	$p_{\text{in}}$	$\bar{C}_{\theta\theta\theta\theta}$	$\bar{C}_{zzzz}$	$\bar{C}_{\theta z \theta z}$	$\bar{C}_{\theta z \theta z}$
planar	0	117	296	106	469
cylindrical	100	558	844	505	1860

**Table 3**

Volume averages  $\bar{g}_\eta = G_\eta/V$  (in mN) for two different internal pressures  $p_{\text{in}}$  (in mmHg). The angle  $\eta$  ranges from  $0^\circ$  ( $\mathbf{e}_\parallel$  in the tangential direction) to  $90^\circ$  ( $\mathbf{e}_\parallel$  in the axial direction).

$p_{\text{in}}$	$\bar{g}_{0^\circ}$	$\bar{g}_{10^\circ}$	$\bar{g}_{20^\circ}$	$\bar{g}_{30^\circ}$	$\bar{g}_{40^\circ}$
0	7.85	14.20	22.64	31.87	39.86
100	15.30	26.20	39.84	53.85	65.03
$p_{\text{in}}$	$\bar{g}_{50^\circ}$	$\bar{g}_{60^\circ}$	$\bar{g}_{70^\circ}$	$\bar{g}_{80^\circ}$	$\bar{g}_{90^\circ}$
0	44.52	44.49	39.67	31.29	21.43
100	70.37	68.24	59.03	45.06	29.71

be used in the calculation of  $\tau$ .

#### 3.2. Meshing geometry

The value of the linear spring stiffnesses depend on  $a_\theta$ ,  $a_z$ ,  $b_\theta$ ,  $b_z$ ,  $c_\theta$ , and  $c_z$ , i.e. they depend on the size, shape, and orientation of the triangle. A right triangle with the catheters parallel to the axis  $\mathbf{e}_\theta$  and to the axis  $\mathbf{e}_z$  is particularly simple to analyze. Let  $a_\theta = a$ ,  $a_z = 0$ ,  $b_\theta = 0$ ,  $b_z = b$ ,  $c_\theta = a$ , and  $c_z = -b$  be the vertex coordinates. The solutions of (15a) and (15b) are

$$\kappa_a = \frac{F_{\theta\theta\theta\theta} + F_{\theta z \theta z}}{a^2}, \quad \kappa_b = \frac{F_{zzzz} + F_{\theta z \theta z}}{b^2}, \quad \kappa_c = 0, \quad (25a)$$

and

$$\chi_\alpha = -\frac{c^2}{a^2} F_{\theta z \theta z}, \quad \chi_\beta = -\frac{c^2}{b^2} F_{\theta z \theta z}, \quad \chi_\gamma = F_{\theta z \theta z} + F_{\theta z \theta z}, \quad (25b)$$

respectively. Furthermore, the deviations  $\Delta\alpha$ ,  $\Delta\beta$ ,  $\Delta\gamma$  in a right triangle can be written as a linear combination of  $\Delta a$ ,  $\Delta b$ ,  $\Delta c$

$$\begin{aligned} \Delta\alpha &= \frac{c}{bc} \Delta a - \frac{\Delta c}{bc}, \\ \Delta\beta &= \frac{c}{ac} \Delta b - \frac{\Delta c}{ac}, \\ \Delta\gamma &= \frac{c}{ab} \Delta c - \frac{\Delta a}{ab} - \frac{\Delta b}{ab}. \end{aligned} \quad (26)$$

Substituting (25a)-(26) in (13), the following result is obtained

$$\begin{aligned} U_{\text{stretch}} &= \frac{1}{2} F_{\theta\theta\theta\theta} \left( \frac{\Delta a}{a} \right)^2 + F_{\theta z \theta z} \frac{\Delta a}{a} \frac{\Delta b}{b} + \frac{1}{2} F_{zzzz} \left( \frac{\Delta b}{b} \right)^2 \\ &\quad + \frac{1}{2} F_{\theta z \theta z} \left( \frac{\Delta a}{b} + \frac{\Delta b}{a} - \frac{c}{ab} \Delta c \right)^2. \end{aligned} \quad (27)$$

Since the stiffness tensor  $C_{ijkl}$  is positive definite, it follows that  $F_{ijkl}$  (proportional to the volume average of  $C_{ijkl}$ , see (14a)) is also positive definite. Thus,  $U_{\text{stretch}}$  is positive for arbitrary deformations, even though  $\kappa_c = 0$  and  $\chi_\alpha$ ,  $\chi_\beta$  are negative.

In general, a triangle is specified by the length of three sides, or two sides and one angle, or one side and two angles, so that the deviations  $\Delta a$ ,  $\Delta b$ ,  $\Delta c$ ,  $\Delta\alpha$ ,  $\Delta\beta$ ,  $\Delta\gamma$  are not independent. This is evident from (11) and (12) where  $\varepsilon_{\theta\theta}$ ,  $\varepsilon_{zz}$ ,  $\varepsilon_{\theta z}$  are used as three independent parameters to specify the deformation. As a result, a combination of more than one spring stiffnesses always appears. Although  $\kappa_a$ ,  $\kappa_b$ ,  $\kappa_c$ ,  $\chi_\alpha$ ,  $\chi_\beta$ ,  $\chi_\gamma$  may not all be positive, the sum in (13) is indeed positive.

Scaling the triangle by a factor  $s$  does not change  $\kappa_a$ ,  $\kappa_b$ , and  $\kappa_c$  in (15a), because  $F_{ijkl}$  in (14a) is proportional to the volume i.e. to  $s^3$  for a constant thickness. On the other hand, from (15b) it follows that  $\chi_\alpha$ ,  $\chi_\beta$ , and  $\chi_\gamma$  are proportional to  $s^2$ . Hence, the sign and the ratio among the

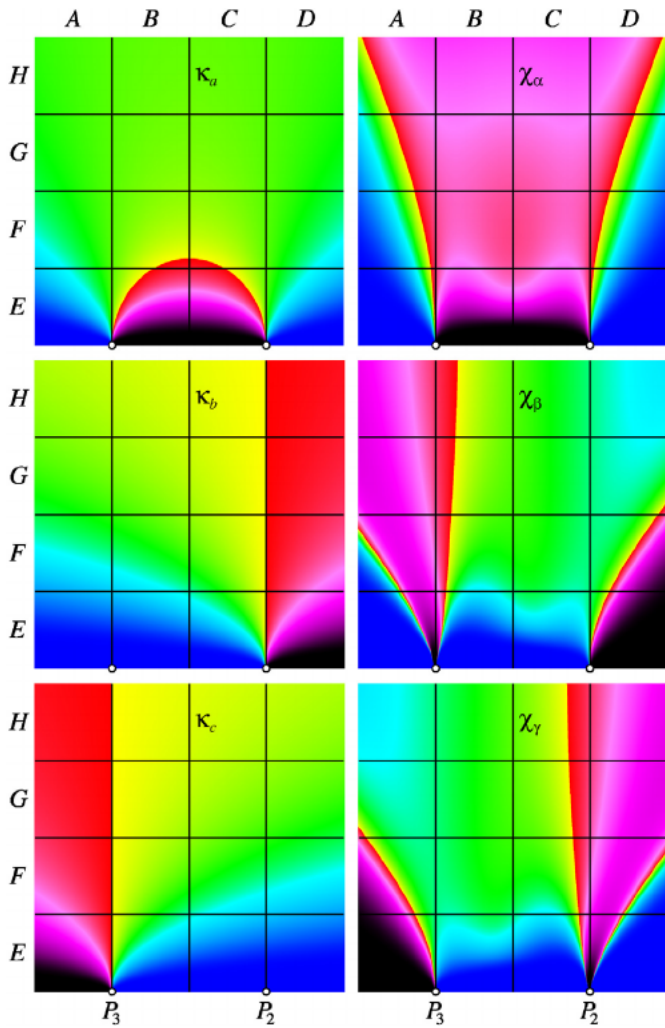


Fig. 4. Spring stiffnesses  $\kappa_a, \kappa_b, \kappa_c, \chi_\alpha, \chi_\beta,$  and  $\chi_\gamma$  as function of the triangle shape for  $\Omega = 0^\circ$  (see Fig. 2(a)). The vertices  $P_2$  and  $P_3$  of the triangle are located at the white dots at the bottom of each graphic. The stiffnesses depend on the relative position of the vertex  $P_1$ , i.e. on  $b_\theta$  and  $b_z$ . A negative stiffness starts from red, to magenta, and then to black (the minimum). A positive stiffness starts from yellow, to green, and then to blue (the maximum). The letters A, B, C, D label four columns and the letters E, F, G, H label four rows. (For interpretation of the references to colour in this figure legend, the reader is referred to the Web version of this article.)

spring stiffnesses does not depend on the scaling factor and they are determined by the shape and orientation of the triangle.

In other words, only  $a_\theta : a_z : b_\theta : b_z : c_\theta : c_z$  matters and since  $(c_\theta, c_z) = (a_\theta, a_z) - (b_\theta, b_z)$ , there are three independent parameters. Let  $a_\theta = \cos \Omega$  and  $a_z = \sin \Omega$  (i.e. set the length  $a = 1$ ), where the angle  $\Omega$  determines the orientation of the triangle (Fig. 2). Then the relative spring stiffnesses become functions of  $\Omega, b_\theta$ , and  $b_z$ .

For instance, consider the data in Table 2 for  $p_{in} = 100$  mmHg. Because  $F_{ijkl} = \nu C_{ijkl}$ , the following ratio is obtained  $F_{\theta\theta\theta\theta} : F_{\theta z z z} : F_{z z z z} : F_{\theta z \theta z} = 1.104 : 1 : 1.670 : 3.682$ .

Figure 4 shows the stiffnesses for  $\Omega = 0^\circ$  as function of  $b_\theta$  (abscissa) and  $b_z$  (ordinate). The coordinate  $b_\theta = b_z = 0$  corresponds to the point  $P_3$  at the left and  $c_\theta = c_z = 0$  corresponds to the point  $P_2$  at the right. It is a simple task to verify that for  $a_z = 0$ , the Eqs. (15a) and (15b) are invariant under the replacements  $b_\theta \leftrightarrow c_\theta, \kappa_b \leftrightarrow \kappa_c, \chi_\beta \leftrightarrow \chi_\gamma$ . This fact explains the symmetries observed in Fig. 4.

The shape of the triangles is arbitrary and any point  $P_1$  can be used as a vertex. Although the spring stiffnesses exhibit wide variations, (13) and (14) will always coincide when the deformations are small.

However, mixing large positive and large negative spring stiffnesses can induce significant errors in the numerical calculations.

Thus, the black and the blue regions in Fig. 4 should be avoided. These regions (square label E) correspond to the cases when the angles  $\beta$  or  $\gamma$  are small.

Physically, in a skinny triangle the elastic restoring forces between the nodes can be very large so that the deformation does not increase too much when an external force is applied.

The most convenient choice of the spring stiffness is obtained when  $\kappa_a, \kappa_b, \kappa_c$  are of the same order. It can be seen in Fig. 4 that this is verified next to the central line (between the squares B and C) and not close to the E squares. In particular, the solution  $\kappa_a = \kappa_b = \kappa_c$  is achieved when

$$\frac{b_z}{a_\theta} = \frac{\sqrt{3}}{2} \left( \frac{F_{zzzz} + F_{\theta\theta zz}}{F_{\theta\theta\theta\theta} + F_{\theta\theta\theta z}} \right)^{1/2}.$$

In the specific example considered here, the outcome is

$$\frac{b_z}{a_\theta} = 1.1265 \frac{\sqrt{3}}{2} = 0.9756, \tag{28}$$

i.e. the height of the isosceles triangle is almost equal to the width. An equilateral triangle would result if  $b_z/a_\theta = \sqrt{3}/2$ , i.e. for an isotropic material ( $F_{zzzz} = F_{\theta\theta\theta\theta} = F_{\theta\theta zz} + 2F_{\theta z \theta z}$ ). In this case, the spring stiffnesses are  $\kappa_a = \kappa_b = \kappa_c = \frac{4}{3}(F_{\theta\theta zz} + F_{\theta z \theta z})/a_\theta^2$  and  $\chi_\alpha = \chi_\beta = \chi_\gamma = \frac{4}{9}(F_{\theta z \theta z} - F_{\theta\theta zz})$ .

It is also convenient to have  $\chi_\alpha, \chi_\beta, \chi_\gamma$  positive and of the same order. This cannot be fulfilled for  $\chi_\alpha$  in Fig. 4, which is negative next to the central vertical line. However, the positive  $\chi_\beta$  and  $\chi_\gamma$  overcome the negative  $\chi_\alpha$  and fix the problem. When the base is parallel to the main axis, it is more advantageous to take an isosceles triangle with a base length similar to the height.

It is interesting to see what happens when  $\Omega \neq 0^\circ$ , i.e. the segment  $P_2P_3$  in Fig. 2(a) is not parallel to the tangential direction. This can occur e.g. when meshing an irregular surface. Fig. 5 shows the result for  $\Omega = 10^\circ$  and it can be seen that the symmetries in Fig. 4 are lost. The original orientation with respect to the tangential axis can be recovered, if the displacement to the next set of nodes is not perpendicular to the base but is rotated clockwise  $10^\circ$ .

### 3.3. Angular spring $\tau$

The bending energy of a beam depends on the curvature. According to (16) and (17) it is proportional to  $[f(\varphi)]^2$ , where

$$f(\varphi) = 2 \left( \sin \frac{\varphi}{2} - \sin \frac{\varphi_0}{2} \right) \tag{29}$$

The function  $f(\varphi)$  can be expanded in powers of  $\sin \varphi - \sin \varphi_0$

$$\begin{aligned} f(\varphi) &= \frac{\cos \frac{\varphi_0}{2}}{\cos \varphi_0} (\sin \varphi - \sin \varphi_0) + \sin \frac{\varphi_0}{2} \frac{2 + \cos \varphi_0}{4 \cos^3 \varphi_0} (\sin \varphi - \sin \varphi_0)^2 + \dots \\ &\approx \frac{\cos \frac{\varphi_0}{2}}{\cos \varphi_0} (\sin \varphi - \sin \varphi_0) = f_s(\varphi), \end{aligned} \tag{29a}$$

or in powers of  $\cos \varphi_0 - \cos \varphi$

$$\begin{aligned} f(\varphi) &= \frac{\cos \varphi_0 - \cos \varphi}{2 \sin \frac{\varphi_0}{2}} - \frac{(\cos \varphi_0 - \cos \varphi)^2}{16 \sin^3 \frac{\varphi_0}{2}} + \dots \\ &\approx \frac{\cos \varphi_0 - \cos \varphi}{2 \sin \frac{\varphi_0}{2}} = f_c(\varphi). \end{aligned} \tag{29b}$$

Comparing (29a) and (29b) for small  $\varphi_0$ , it can be seen that the approximation  $f_s(\varphi)$  is better than  $f_c(\varphi)$ . On the other hand, for  $\varphi_0 \sim 90^\circ$  the approximation  $f_c(\varphi)$  is better than  $f_s(\varphi)$ .

Fig. 6 shows a comparison of  $[f(\varphi)]^2$  with the approximations  $[f_c(\varphi)]^2$  and  $[f_s(\varphi)]^2$  for some selected values of  $\varphi_0$ . For  $0^\circ < \varphi_0 < 45^\circ$  the blue curve gives a better approximation to the green curve (Fig. 6(b)),

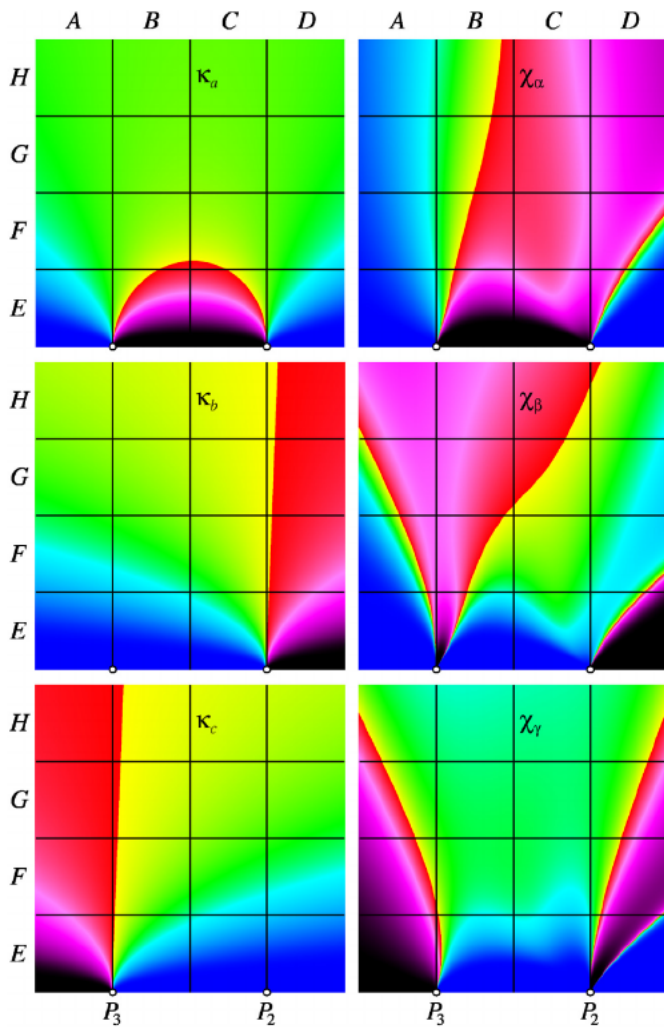


Fig. 5. Same as in Fig. 4, but the base of the triangle is tilted by an angle  $\Omega = 10^\circ$  with respect to the tangential direction.

but for  $45^\circ < \varphi_0 < 90^\circ$  the red curve gives a better approximation to the green curve (Fig. 6(d)). At  $\varphi_0 = 45^\circ$  the approximation  $[f_c(\varphi)]^2$  is as good as  $[f_s(\varphi)]^2$  (Fig. 6(c)).

Since  $[f_c(\varphi)]^2$  is an even function of  $\varphi$ , there are two equivalent equilibrium positions (minima) at  $\varphi = \pm\varphi_0$ . A closer look reveals that  $[f_c(\varphi)]^2$  is a double well separated by a barrier which is small when  $\varphi_0$  is close to  $0^\circ$ . On the other hand,  $[f(\varphi)]^2$  has a single minimum at  $\varphi = \varphi_0$  and so  $[f_c(\varphi)]^2$  is a bad approximation when  $\varphi_0$  is small. A similar problem arises for  $[f_s(\varphi)]^2$  when  $\varphi_0$  is close to  $90^\circ$ .

In the special case  $\varphi_0 = 90^\circ$ , Eq. (29a) is no longer valid and the square of  $f_s(\varphi)$  must be replaced by

$$[f_{s0}(\varphi)]^2 = 1 - \sin\varphi. \quad (29c)$$

Further, when  $\varphi_0 = 0^\circ$  the square of (3.3) must be replaced by

$$[f_{c0}(\varphi)]^2 = 2(1 - \cos\varphi), \quad (29d)$$

which is identical to  $4\sin^2(\varphi/2) = [f(\varphi)]^2$  (see (29) with  $\varphi_0 = 0^\circ$ ). The transition between  $[f_s(\varphi)]^2$  and  $[f_{s0}(\varphi)]^2$  (the blue curve in Fig. 6(d) and (e)) is abrupt and the same conclusion holds for  $[f_c(\varphi)]^2$  and  $[f_{c0}(\varphi)]^2$ . In a biological tissue, a surface with a small  $\varphi_0$  is much more common than a surface with  $\varphi_0 \sim 90^\circ$  (a right angle corner). Hence, it is better to apply (18) rather than Eq. (21) of Ref. (Baier-Saip et al., 2017).

### 3.4. Comparison

In what follows, consider a cylindrical artery as described in Section

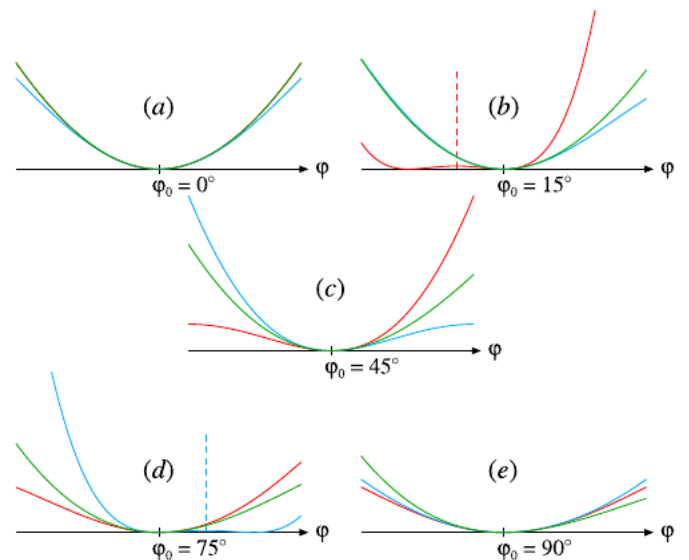


Fig. 6. Functions  $[f(\varphi)]^2$  (green),  $[f_c(\varphi)]^2$  (red), and  $[f_s(\varphi)]^2$  (blue) in the interval  $\varphi_0 - 45^\circ < \varphi < \varphi_0 + 45^\circ$ , for different values of  $\varphi_0$ . The function  $[f_{c0}(\varphi)]^2$  replaces  $[f_c(\varphi)]^2$  in (a), and the function  $[f_{s0}(\varphi)]^2$  replaces  $[f_s(\varphi)]^2$  in (e). Remark that in (a) the red curve (not shown) coincides with the green curve. Further, in (b) the red curve is symmetric with respect to the broken line at  $\varphi = 0^\circ$  and in (d) the blue curve is symmetric with respect to the broken line at  $\varphi = 90^\circ$ . (For interpretation of the references to colour in this figure legend, the reader is referred to the Web version of this article.)

3.1, with an initial pressure of 100 mmHg and an internal radius  $r_1 = 1.55$  mm. The cylinder is discretized by a polyline having  $N = 24$  vertices in the tangential direction. The meshing geometry corresponds to isosceles triangles with a base of dimension  $a_\theta = 2r_1\sin(2\pi/2N) = 0.405$  mm and a height  $b_z = 0.395$  mm (see (28)). Using (15a), (15b), and (21c) the following spring stiffnesses are obtained:  $\kappa_a = \kappa_b = \kappa_c = 362$  N/m,  $\chi_\alpha = -81.4$   $\mu$ J,  $\chi_\beta = \chi_\gamma = 105.6$   $\mu$ J,  $\tau_a = 31.98$   $\mu$ J (rotation axis along side  $a$ , see Fig. 2),  $\tau_b = \tau_c = 65.46$   $\mu$ J (rotation axis along side  $b$  or side  $c$ ).

The results with the new model have the label D and with the previous model have the label A. As a reference, the calculations with the nonlinear incompressible artery model of Holzapfel et al. (2005) (label B) are also given. Since the tests performed to validate the calculations are the same as those in Ref. (Baier-Saip et al., 2017), they will be only briefly described.

**Pressure-inflation.** The inflation is the most common artery deformation. In this case, there is no axial displacement and the essential parameter describing the deformation is the tangential stretch. When the pressure varies between 80 and 120 mm Hg, the average stretch calculated with model D is in the interval [1.080123, 1.096196]. The corresponding result with model A is [1.080073, 1.096222] and with model B is [1.080286, 1.093868] (see Fig. 8 of Ref. (Baier-Saip et al., 2017)). Hence, the difference between models A and D is marginal.

**Axial force.** The axial direction is also relevant and a test including the axial deformation is performed. The stretch varies from  $\lambda_z = 1$  to  $\lambda_z = 1.01$ , the blood pressure is kept constant at 100 mmHg, and the radius is not fixed. Note that when the artery is axially stretched, it becomes stiffer, and the internal radius becomes smaller (Baier-Saip et al., 2017). Table 4 shows that the axial force and the variation of  $r_1$  are similar in the three models.

**Bending.** Since the model is essentially a two-dimensional mesh, it is important to examine deformations in the perpendicular direction. Consider a planar slice with a rectangular shape. In order to compare the deformations with those in Ref. (Baier-Saip et al., 2017), the same geometrical dimensions  $a_\theta = 0.405$  mm,  $b_z = 0.449$  mm are used. The slice hangs horizontally from two opposite edges (see Fig. 9 of Ref. (Baier-Saip et al., 2017)) and it is subjected to a vertical pressure load of

**Table 4**

Force  $F_z$  and internal radius  $r_1$  for a stretch  $\lambda_z = 1.01$  and a pressure equal to 100 mmHg. In all cases the initial radius is 1.5518 mm and  $\Delta r_1$  represents the percentage decrease of the radius when the axial stretch varies from 1 to 1.01.

Model	$F_z$	$r_1$	$\Delta r_1$
A	0.03971 N	1.5377 mm	- 0.91%
B	0.03633 N	1.5351 mm	- 1.08%
D	0.04195 N	1.5381 mm	- 0.88%

200 Pa. The stiffness tensor corresponds to  $p_{in} = 0$  in Table 2 and the spring stiffnesses are  $\kappa_a = 90.85$  N/m,  $\kappa_b = \kappa_c = 71.80$  N/m,  $\chi_\alpha = -17.59$   $\mu$ J,  $\chi_\beta = \chi_\gamma = 19.59$   $\mu$ J,  $\tau_a = 15.28$   $\mu$ J,  $\tau_b = \tau_c = 31.69$   $\mu$ J.

The calculated axial length  $L_D = 8.71$  mm is almost equal to the length  $L_A = 8.72$  mm obtained previously. Moreover, the modulus of the maximum beam deflections are  $\delta_{maxD} = 0.8239$  mm and  $\delta_{maxA} = 0.8145$  mm. As a reference, the analytical value obtained with Eq. (44) of Ref. (Baier-Saip et al., 2017) is  $\delta_{max,ana} = 0.7795$  mm. The difference between  $\delta_{maxA}$  and  $\delta_{max,ana}$  is 4.5%, and it increases slightly to 5.7% between  $\delta_{maxD}$  and  $\delta_{max,ana}$ . Observe that the outcome with model A is better because for  $\varphi_0 = 0^\circ$  the approximation  $f_{c0}(\varphi)$  is exact. On the other hand, if the initial slice is slightly bended ( $\varphi_0 \approx 0^\circ$ ), then  $f_c(\varphi)$  must be used in place of  $f_{c0}(\varphi)$  and in this case the approximation is worse than  $f_s(\varphi)$  of model D.

### 3.5. Variable stiffness

Collagen exhibits high nonlinear behavior bearing the major part of the load transmitted through the tissue, while elastin has important flexibility and extensibility features for blood vessels (Saez et al., 2014). At low stretch, the elastin is the sole load-bearing component, but at high stretch the collagen bears the main load (Holzapfel et al., 2000). If the stretch becomes very high, the elastin can rupture and this drastically changes the elastic properties in the low stretch domain. As a result, the artery can bear a moderate load only if the stretch is large, and so it becomes permanently deformed giving rise to the aneurysm (Drangova et al., 1993; Wulandana and Robertson, 2005).

As an example, consider a cylindrical arterial segment which is not homogeneous. Specifically, the parameter  $k'_{2t}$  in the free energy  $\Psi_t$  is replaced by

$$k'_{2t} = k_{2t} \left( 1 - \frac{e^{-z^2/\sigma^2}}{2} \right) \quad (30)$$

with  $\sigma = 2.964$  mm. Hence, at  $z = 0$  the parameter  $k'_{2t}$  is reduced to 50% of  $k_{2t}$  and for  $|z| > \sigma$  the parameter  $k'_{2t}$  approaches to  $k_{2t}$ . The smaller  $k'_{2t}$  causes a decrease in the stiffness and it represents, in a simplified way, an artery with fusiform aneurysm.

The problem formulated above has an axial symmetry and the stretch in model B is calculated as in Ref. (Baier-Saip et al., 2017) but with a variable  $k_{2t}$ . Since the radius depends on  $z$ , the axial stretch

$$\lambda_z = \sqrt{1 + \left( \frac{dr_1}{dz} \right)^2} \quad (31)$$

becomes a function of  $z$ . The first integration is carried out with  $\lambda_z = 1$  to find an approximation for  $\eta(z)$ . Then a new  $\lambda_z$  is calculated with (31), and the procedure is repeated until convergence is achieved.

The same problem is solved with model D. When the internal pressure equals 100 mmHg, the artery is not a right circular cylinder, but it is slightly expanded at the center. Thus, the initial geometry of the triangles varies with the coordinate  $z$ . Since  $k'_{2t}$  decrease at the center, the stretches  $\lambda_\theta$  and  $\lambda_z$  must increase in order to balance the stiffness. An explicit calculation shows that the overall effect is a net decrease in the stiffness tensor and so in the spring stiffnesses. However, a small increase in the pressure results in a larger variation of the stretch and the stiffness in the nonlinear model increases abruptly.

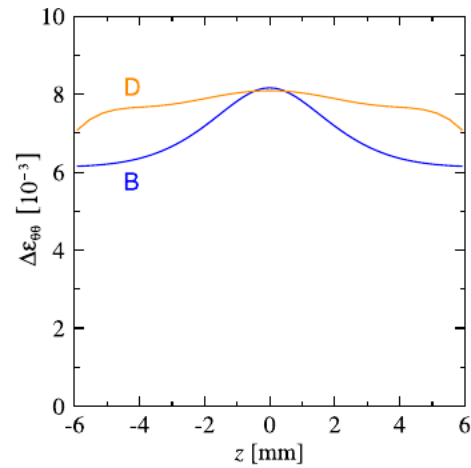


**Fig. 7.** Tangential strain variation  $\Delta\varepsilon_{\theta\theta}$  when the pressure increases from 90 mmHg to 110 mmHg. The artery segment has a cylindrical symmetry in the unloaded state but the physical properties depend on the coordinate  $z$  (see (30)). The blue curve corresponds to the calculations performed with the nonlinear model B and the orange curve corresponds to the calculations performed with the model D developed in this work. (For interpretation of the references to colour in this figure legend, the reader is referred to the Web version of this article.)

Fig. 7 shows the variation of the tangential strain  $\Delta\varepsilon_{\theta\theta}$  using model B and using model D. Close to the borders  $k'_{2t} \rightarrow k_{2t}$  and  $(\Delta\varepsilon_{\theta\theta})_D > (\Delta\varepsilon_{\theta\theta})_B$ , in accordance with Fig. 8 of Ref. (Baier-Saip et al., 2017) where the stretch variation is slightly bigger in the linearized model A. In regions where  $k'_{2t}$  is smaller,  $(\Delta\varepsilon_{\theta\theta})_D < (\Delta\varepsilon_{\theta\theta})_B$  results. The model B is more sensitive to variations of the physical parameters, because it is nonlinear.

Lastly, note that the strain in Fig. 7 is smaller than 1%, and the agreement between models B and D is good. But for wider variations of the internal pressure or smaller values of  $k_{2t}$ , the strain increases and the linear approximation (model D) is no longer valid (Baier-Saip et al., 2017).

## 4. Conclusions

The artery model developed in this work is linear, two-dimensional, and it is suitable for computing small and noninvasive artery deformations. The model incorporates the individual characteristics of each arterial tissue, but in the present work residual stresses are not taken into account. Additional stiffness tensor components have been computed and three kinds of springs are used to describe the interactions between the nodes of the 2D mesh.

The stiffnesses of the normal spring  $\kappa$  and of the angular in plane spring  $\chi$ , are derived by comparing the elastic energy stored in the springs and the energy in the layers subjected to the same plane strain. The determination of the angular out of plane spring stiffness  $\tau$  is carried out by comparing the energies when the tissues are bent. The spring  $\tau$  is essential for the stability of the two-dimensional structure, otherwise the stiffness matrix becomes singular. In particular, a single out of plane spring  $\tau$  replaces the two springs  $\tau_{old}$  and the two springs  $\zeta_{old}$  of the previous work (Baier-Saip et al., 2017). As a result, the abrupt transition between  $\tau_{old}$  and  $\zeta_{old}$  close to  $\varphi_0 = 0$  does not longer appear.

The actual procedure is more flexible than the previous one, mainly because the meshing is based on triangles rather than on quadrilaterals. The elastic properties of the arteries are better represented in the present work, as more components of the stiffness tensor have been included in the model. These components have not been measured but only estimated. Nevertheless, their exact value is not important as long as they do not appear in the energy of the deformation being considered. For example, in a pure axial stretch there is no shear strain and

the value of  $C_{\alpha\beta\gamma\delta}$  is immaterial.

Different loads validated the model. The first one evaluated the most relevant case, where the blood pressure inflates the artery, and the outcome was close to the nonlinear and incompressible artery. When the artery is stretched by a small amount in the axial direction, the calculations with all models also led to similar results. Finally, after the stiffness tensor has been calculated, it is straightforward to apply the method to arteries with irregular surface geometry.

## Acknowledgements

This work was supported by Conselho Nacional de Desenvolvimento Científico e Tecnológico (CNPq, projects 454815/2015-8, 573710/2008-2) and Fundação de Amparo à Pesquisa do Estado do Rio de Janeiro (FAPERJ, project E-26/170.030/2008).

## References

- Alderliesten, T., Konings, M.K., Niessen, W.J., 2007. Modeling friction, intrinsic curvature, and rotation of guide wires for simulation of minimally invasive vascular interventions. *IEEE Trans. Biomed. Eng.* 54, 29–38.
- Baier, P.A., Srinivasan, L., Baier-Saip, J.A., Voelker, W., Schilling, K., 2015. Surfaces for modeling arteries in virtual reality simulators. *IFAC-PapersOnLine* 48, 031–036.
- Baier, P.A., Baier-Saip, J.A., Schilling, K., Oliveira, J.C., 2016. Simulator for minimally invasive vascular interventions: hardware and software. *Presence* 25, 108–128.
- Baier-Saip, J.A., Baier, P.A., Schilling, K., Oliveira, J.C., 2017. Approximate artery elasticity using linear springs. *J. Med. Biol. Eng.* 37, 899–911.
- Cilla, M., Peña, E., Martínez, M.A., 2012. 3D computational parametric analysis of eccentric atheroma plaque: influence of axial and circumferential residual stresses. *Biomech Model Mechanobiol* 11, 1001–1013.
- Creane, A., Maher, E., Sultan, S., Hynes, N., Kelly, D.J., Lally, C., 2010. Finite element modelling of diseased carotid bifurcations generated from in vivo computerized tomographic angiography. *Comput. Biol. Med.* 40, 419–429.
- Diez, J., 2007. Arterial stiffness and extracellular matrix. *Adv. Cardiol.* 44, 76–95.
- Drangova, M., Holdsworth, D.W., Boyd, C.J., Dunmore, P.J., Roach, M.R., Fenster, A., 1993. Elasticity and geometry measurements of vascular specimens using a high-resolution laboratory CT scanner. *Physiol. Meas.* 14, 277–290.
- Fung, Y.C., 1991. What are the residual stresses doing in our blood vessels? *Ann. Biomed. Eng.* 19, 237–249.
- Fung, Y.C., 1993. *Biomechanics: Mechanical Properties of Living Tissues*. Springer.
- García, M., Mendoza, C., Pastor, L., Rodríguez, A., 2006. Optimized linear FEM for modeling deformable objects. *Comput. Animat. Virtual Worlds* 17, 393–402.
- García-Herrera, C.M., Celentano, D.J., Cruchaga, M.A., Rojo, F.J., Atienza, J.M., Guinea, G.V., Goicole, J.M., 2012. Mechanical characterization of the human thoracic descending aorta: experiments and modelling. *Comput. Meth. Biomech. Biomed. Eng.* 15, 185–193.
- Gasser, T.C., Ogden, R.W., Holzapfel, G.A., 2006. Hyperelastic modelling of arterial layers with distributed collagen fibre orientations. *J. R. Soc. Interface* 3, 15–35.
- Gwak, K.W., Paden, B.E., Antaki, J.F., Ahn, I.S., 2010. Experimental verification of the feasibility of the cardiovascular impedance simulator. *IEEE Trans. Biomed. Eng.* 57, 1176–1183.
- Holzapfel, G.A., Ogden, R.W., 2009. In planar biaxial tests for anisotropic nonlinearly elastic solids. A continuum mechanical framework. *Math. Mech. Solid* 14, 474–489.
- Holzapfel, G.A., Ogden, R.W., 2010. Constitutive modelling of arteries. *Proc R Soc A* 466, 1551–1597.
- Holzapfel, G.A., Ogden, R.W., 2017. On fiber dispersion models: exclusion of compressed fibers and spurious model comparisons. *J. Elast* 129, 49–68.
- Holzapfel, G.A., Gasser, T.C., Ogden, R.W., 2000. A new constitutive framework for arterial wall mechanics and a comparative study of material models. *J. Elast* 61, 1–48.
- Holzapfel, G.A., Gasser, T.C., Stadler, M., 2002. A structural model for the viscoelastic behavior of arterial walls: continuum formulation and finite element analysis. *European J Mech A/Solids* 21, 441–463.
- Holzapfel, G.A., Sommer, G., Gasser, C.T., Regitnig, P., 2005. Determination of layer-specific mechanical properties of human coronary arteries with nonatherosclerotic intimal thickening and related constitutive modeling. *Am. J. Physiol. Heart Circ. Physiol.* 289, H2048–H2058.
- Holzapfel, G.A., Mulvihill, J.J., Cunnane, E.M., Walsh, M.T., 2014. Computational approaches for analyzing the mechanics of atherosclerotic plaques: a review. *J. Biomech.* 47, 859–869.
- Holzapfel, G.A., Niestrawska, J.A., Ogden, R.W., Reinisch, A.J., Schrief, A.J., 2015. Modelling non-symmetric collagen fibre dispersion in arterial walls. *J. R. Soc. Interface* 12, 20150188.
- Humphrey, J.D., 2002. *Cardiovascular Solid Mechanics: Cells, Tissues, and Organs*. Springer-Verlag.
- Lanir, Y., 1983. Constitutive equations for fibrous connective tissues. *J. Biomech.* 16, 1–12.
- Li, W., 2016. Damage models for soft tissues: a survey. *J. Med. Biol. Eng.* 36, 285–307.
- Misra, S., Ramesh, K.T., Okamura, A.M., 2008. Modeling of tool-tissue interactions for computer-based surgical simulation: a literature review. *Presence (Camb)* 17, 463.
- Morlacchi, S., Colleoni, S.G., Cardenes, R., Chiastra, C., Diez, J.L., Larrabide, I., Migliavacca, F., 2013. Patient-specific simulations of stenting procedures in coronary bifurcations: two clinical cases. *Med. Eng. Phys.* 35, 1272–1281.
- Pereira, T., Correia, C., Cardoso, J., 2015. Novel methods for pulse wave velocity measurement. *J. Med. Biol. Eng.* 35, 555–565.
- Pierce, D.M., Fastl, T.E., Rodríguez-Vila, B., Verbrugge, P., Fourneau, I., Maleux, G., Herijgers, P., Gomez, E.J., Holzapfel, G.A., 2015. A method for incorporating three-dimensional residual stretches/stresses into patient-specific finite element simulations of arteries. *J Mech Behav Biomed Mater* 47, 147–164.
- Saez, P., Pena, E., Martínez, M.A., 2014. A structural approach including the behavior of collagen cross-links to model patient-specific human carotid arteries. *Ann. Biomed. Eng.* 42, 1158–1169.
- Schmid, H., Grytsan, A., Poshtan, E., Watton, P.N., Itskov, M., 2013. Influence of differing material properties in media and adventitia on arterial adaptation application to aneurysm formation and rupture. *Comput Methods Biomech Biomed Eng* 16, 33–53.
- Sokolis, D.P., 2008. Passive mechanical properties and constitutive modeling of blood vessels in relation to microstructure. *Med. Biol. Eng. Comput.* 46, 1187–1199.
- Vito, R.P., Dixon, S.A., 2003. Blood vessel constitutive models: 1995–2002. *Annu. Rev. Biomed. Eng.* 5, 413–439.
- Wang, Y., Guo, S., Tamiya, T., Hirata, H., Ishihara, H., 2014. A blood vessel deformation model based virtual-reality simulator for the robotic catheter operating system. *Neurosci Biomed Eng* 2, 126–131.
- Wulandana, R., Robertson, A.M., 2005. An inelastic multi-mechanism constitutive equation for cerebral arterial tissue. *Biomech Model Mechanobiol* 4, 235–248.
- Zannoli, R., Corazza, I., Branzi, A., 2009. Mechanical simulator of the cardiovascular system. *Phys. Med.* 25, 94–100.